Long-lived coherence between ground and Rydberg levels in a magic-wavelength lattice

J. Lampen, H. Nguyen, L. Li, P. R. Berman, and A. Kuzmich
Department of Physics, University of Michigan, Ann Arbor, Michigan 48109, USA

By confining atoms in a state-insensitive optical lattice, the lifetime of the ground-state–Rydberg coherence is increased to $\geqslant 20\ \mu$s, an order of magnitude improvement over previous experiments using freely diffusing atoms. Using these enhanced lifetimes, we measure the so-called magic lattice wavelengths for Rb and use them to extract the $6p_{3/2}$-$ns_{1/2}$ reduced electric dipole matrix elements. Good agreement is found with values obtained using an effective one-electron potential for principal quantum numbers n between $n = 30$ and $n = 70$. We develop a theoretical model based on quantized motion to map out the ground-state–Rydberg coherence as a function of time that is in good agreement with the experimental results. The availability of long coherence times may present new opportunities for high-resolution spectroscopy and quantum information science.

I. INTRODUCTION

Ground-state–Rydberg-state coherence in ensembles of ultracold atoms plays a critical role in many quantum information, quantum communication, and precision metrology protocols [1–8]. Single-photon generation [9], many-body Rabi oscillations [10], photon antibunching [11], creation of entanglement of light and atomic excitations [12], single-photon optical switches, and interaction-induced phase shifts [13–17] have been demonstrated based on coupling of ensembles of neutral atoms with propagating quantum light fields. Significant progress has also been made in employing Rydberg interactions for entanglement [18–20], many-body interferometry [21], and quantum simulation in arrays of neutral atoms [22]. All these experiments have relied on quantum coherence between the ground and Rydberg states. Prolonging this coherence lifetime is therefore crucial to further advances in increasing the size and complexity of quantum algorithms and the precision of atomic measurements.

Several physical processes contribute to ground-state–Rydberg decoherence, including spontaneous decay, blackbody radiation, and coupling to stray electric fields [1]. In the majority of experiments to date, however, the loss of coherence can be attributed mainly to motional dephasing, limiting the coherence lifetime to a few microseconds [9,10,18–20,22]. Motional dephasing can be reduced by tightly confining the atoms in an optical dipole trap. Unfortunately, while typical off-resonant dipole traps are attractive for ground-state atoms, they are repulsive for atoms in Rydberg levels. This results in fast decoherence owing to position-dependent differential energy shifts, making it necessary to turn off the trapping fields for the duration of the Rydberg excitation period. To overcome this problem, the trapping fields can be tuned to a so-called magic wavelength [23,24] that results in identical energy shifts for the ground and Rydberg states [12,25]. The magic wavelength is close to that of the Rydberg level $|ns_{1/2}\rangle$ to intermediate level $|6p\rangle$ transition.

In this work we exploit the use of the magic wavelength to obtain a significant enhancement of ground-state–Rydberg atomic coherence lifetimes over a range of principal quantum numbers $n = 30, \ldots, 70$. This is achieved by confining the atomic sample in a one-dimensional, state-insensitive optical lattice along the axis of propagation of the excitation light fields. We observe damped oscillations of the collective ground-state–Rydberg atomic coherence in the lattice potential. The anharmonicity of the potential leads to a damping of the visibility of the oscillations, whereas the radiative decay and blackbody radiation-driven depopulation of the Rydberg state lead to a damping of the overall signal.

A second component of this paper is the formulation of a theory that can be used to explain the overall features of the experimental data. A first-principles calculation of the signal presents considerable challenges, even when interactions between Rydberg atoms can be neglected. The reason for this is that standard methods [26] involving the use of the Maxwell-Bloch equations or a source-field approach are no longer applicable when the atoms undergo quantized motion in the trap potentials. Moreover, if the trap potentials differ for the Rydberg- and ground-state potentials, any approach assuming classical motion in the potentials fails if the signal depends on the coherence between these levels. There *have* been theories of phased-matched emission from trapped atoms that have been developed in the context of atom interferometry [27], but the formalisms used in those approaches differ somewhat from what is needed in our problem involving excitation of Rydberg levels. More closely related to our calculations are those of Zhao *et al.* [28] and Jenkins *et al.* [29], who considered phase-matched emission from trapped atoms using Raman transitions. Jenkins *et al.* [29] used a model in which the atoms undergo classical motion in a lattice potential. In contrast to these authors, we present a theory that treats the atomic motion in the lattice quantum mechanically and allows for different Rydberg- and ground-state potentials. We first present a theoretical formalism that can be used to model our system and then describe its experimental implementation.
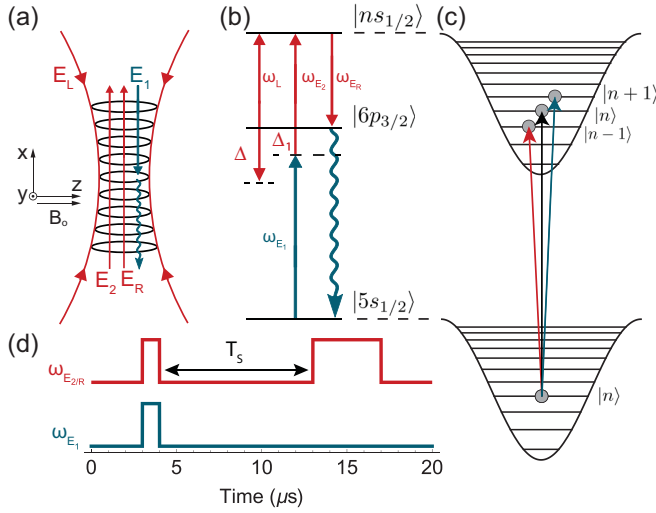
FIG. 1. (a) A cold sample of ^{87}Rb gas is trapped in a 0.5-μm-period one-dimensional optical lattice formed by a retroreflected beam E_L. Two nearly counterpropagating beams E_1 and E_2 excite a spin wave between the $|5s_{1/2}, F = 2\rangle$ and $|ns_{1/2}\rangle$ levels. After a storage time T_s, a retrieval pulse E_R is applied, creating an array of atomic dipoles which give rise to a phase-matched emission from the sample. The actual geometry used in the experiment differs somewhat from that shown schematically in the figure. (b) Relevant ^{87}Rb energy levels and corresponding fields, with $\Delta = \omega_L - \omega_{ns,6p_{3/2}}$ and $\Delta_1 = \omega_{E_2} - \omega_{ns,6p_{3/2}}$. (c) Schematic diagram indicating transitions between the ground- and excited-state motional levels. (d) Timing diagram showing the excitation and retrieval pulse sequence.

II. THEORY

There are essentially three ingredients needed to calculate the signal. First, the ground- and Rydberg-state potentials produced by the trap fields must be obtained. Second, the contribution to the signal at the detector produced by a single atom needs to be derived. Finally, a weighted sum over the contributions from atoms at different points in the trap potential and an average over the thermal distribution in the sample must be carried out. Each atom is modeled as a three-level system with level 1 corresponding to the ground state, level 2 to the $6p_{3/2}$ state, and level 3 to the ns state, as shown in Fig. 1. The atom interacts with both a classical two-photon pulse at time $t = 0$ and a classical readout pulse at time T_s. The applied pulses propagate in the $\pm X$ direction. The first pulse has an effective **k** vector $(k_{E_1} - k_{E_2})\mathbf{u}_x$ and effective two-photon frequency $\omega_{E_{31}} = \omega_{E_1} + \omega_{E_2}$, while the readout pulse has a **k** vector $-k_R\mathbf{u}_x$ and frequency $\omega_R \approx \omega_{E_2}$. As a result of these interactions and the interaction with the vacuum field, a phase-matched signal is generated from the sample.

There is also a trap potential formed by fields counterpropagating in the X direction having wavelength $\lambda_L = 2\pi/k_L = 2\pi c/\omega_L$. The detuning of the trap field frequency from the ns-$6p_{3/2}$ transition frequency is denoted by Δ. The motion of the atoms in the potential wells in the longitudinal direction is treated quantum mechanically, while the motion in the transverse trap potential is treated classically. It is assumed that all the atoms are trapped; transitions to continuum states are not taken into account. Moreover, we neglect any

modifications of the signal resulting from Rydberg-atom–Rydberg-atom interactions.

A. Optical potentials

We need not consider the optical potential associated with state $|2\rangle$ since it drops out of the calculation of the phase-matched signal. To arrive at expressions for the optical potentials for states $|1\rangle$ and $|3\rangle$, we write the y-polarized trap electric-field amplitude as

$$E(\mathbf{R}, t) = \tfrac{1}{4}[A_+(\rho, X)e^{ik_L X} + A_-(\rho, X)e^{-ik_L X}]e^{-i\omega_L t} + \text{c.c.}, \quad (1)$$

where

$$A_\pm(\rho, X) = E_{\pm,0}\frac{w_{\pm,0}}{w_\pm(X)}e^{-\rho^2/w_\pm^2(X)}, \quad (2)$$

ρ is the coordinate transverse to X, $E_{\pm,0}$ are the field amplitudes for the fields propagating in the $\pm X$ directions that constitute the trap, $w_{\pm,0}$ are the waist radii of these fields,

$$w_\pm(X) = w_{\pm,0}\sqrt{1 + \frac{(X - X_{\pm,0})^2}{X_{\pm,r}^2}}, \quad (3)$$

$X_{\pm,r} = \pi w_{\pm,0}^2/\lambda_L$ are Rayleigh lengths, and $X_{\pm,0}$ are the positions of the foci of the beams. We have allowed for unbalanced beams, that is, the beams propagating in the $\pm X$ directions can have different waists and be centered at different positions.

The time-average field intensity is proportional to

$$|\bar{E}(\mathbf{R})|^2 = \tfrac{1}{8}[4A_+A_-\cos^2(k_L X) + (A_+ - A_-)^2]$$

and results in both a transverse (nonlattice) trap potential that is independent of X and a longitudinal (lattice) $\cos^2(k_L X)$ trap potential. The nonlattice potential, which traps the atoms transversely, also results in a spatially dependent light shift that limits the coherence time of the signal. The position of the Rydberg electron in a single atom can be taken as $\mathbf{R} + \mathbf{r}$, where $\mathbf{R} = (\rho, X)$ is the center-of-mass position vector of the atom and $\mathbf{r}$ its relative electronic coordinate.

The ground-state optical potential, calculated in the dipole approximation, is

$$U_g \approx -\tfrac{1}{2}\alpha_g|\bar{E}(\mathbf{R})|^2$$
$$= -\tfrac{1}{16}\alpha_g[4A_+A_-\cos^2(k_L X) + (A_+ - A_-)^2], \quad (4)$$

where α_g is the ground-state polarizability. To find the optical potential associated with an atom in the Rydberg state ns, we break up the interaction potential into a term representing the $\mathbf{A} \cdot \mathbf{p}$ contribution and one representing the A^2 contribution, where $\mathbf{p}$ is the momentum operator associated with the Rydberg electron and $\mathbf{A} = A(\mathbf{R}, t)\mathbf{u}_y$ is the vector potential (which has the same polarization as the electric field) given by

$$A(\mathbf{R}, t) = \frac{ie^{-i\omega_L t}}{4\omega_L}[A_+(\rho, X)e^{ik_L X} + A_-(\rho, X)e^{-ik_L X}] + \text{c.c.}$$

For the $\mathbf{A} \cdot \mathbf{p}$ term we can use the dipole approximation since the major contribution to the sum that determines this contribution originates from the $6p$ intermediate states; however,

for the A^2 term we do *not* make the dipole approximation and set

$$\theta_n = \langle \cos(2k_L x) \rangle_{ns} \tag{5}$$

and $\langle \sin(2k_L x) \rangle_{ns} = 0$, where the average is over electronic coordinates in the ns state. The total optical potential in the ns state can then be written as [30]

$$U_n \approx -\frac{1}{16}[4A_+(\rho, X)A_-(\rho, X)\cos^2(k_L X) + (A_+ - A_-)^2]$$
$$\times \frac{e^2}{\hbar} \sum_{m \neq n} \frac{2|y_{mn}|^2 \omega_{mn}}{\omega_{mn}^2 - \omega_L^2} \left(\frac{\omega_{mn}}{\omega_L}\right)^2$$
$$+ \frac{|\alpha_f|}{16}[4\theta_n A_+ A_- \cos^2(k_L X)$$
$$+ (A_+ - A_-)^2 + 2A_+ A_-(1 - \theta_n)], \tag{6}$$

where the first term is the $\mathbf{A} \cdot \mathbf{p}$ contribution and the second the A^2 contribution. The quantity $\alpha_f = -e^2/m\omega_L^2$ is the free-electron polarizability. For the detunings $\Delta/2\pi \lesssim 4.5$ GHz used in our experiment, the dominant contribution to the summation appearing in Eq. (6) originates from the intermediate $6p_{3/2}$ levels (the $6p_{3/2}$-$6p_{1/2}$ transition frequency is about 2.3 THz). As a consequence, we can approximate

$$\frac{e^2}{\hbar} \sum_{m \neq n} \frac{2|y_{mn}|^2 \omega_{mn}}{\omega_{mn}^2 - \omega_L^2} \left(\frac{\omega_{mn}}{\omega_L}\right)^2 \approx \frac{D_n^2}{6\hbar\Delta}, \tag{7}$$

where

$$D_n = |\langle ns||\hat{d}||6p_{3/2}\rangle| \tag{8}$$

is a reduced matrix element of the dipole moment operator $\hat{\mathbf{d}}$.

From Eqs. (4) and (6), it then follows that the lattice potentials for levels 1 and 3 are

$$U_1^{(l)}(\rho, X) \approx -\frac{1}{4}\alpha_g A_+(\rho, X)A_-(\rho, X)\cos^2(k_L X), \tag{9a}$$

$$U_3^{(l)}(\rho, X) = -\frac{1}{4}A_+(\rho, X)A_-(\rho, X)\cos^2(k_L X)$$
$$\times \left[\frac{D_n^2}{6\hbar\Delta} - |\alpha_f|\theta_n\right] \tag{9b}$$

and the nonlattice potentials are

$$U_1^{(nl)} = -\frac{\alpha_g}{16}(A_+ - A_-)^2, \tag{10a}$$

$$U_3^{(nl)} = -\frac{D_n^2}{96\hbar\Delta}(A_+ - A_-)^2$$
$$+ \frac{|\alpha_f|}{16}[2A_+ A_-(1 - \theta_n) + (A_+ - A_-)^2]. \tag{10b}$$

Experimentally, the detuning Δ can be chosen to equate the lattice potentials of the ground and Rydberg levels; that is, ω_L is adjusted such that

$$\frac{D_n^2}{6\hbar\Delta_{m,n}} = \alpha_g + |\alpha_f|\theta_n, \tag{11}$$

where $\Delta_{m,n}$ is the so-called magic detuning for the ns Rydberg level. In this limit, the difference between the Rydberg-

and ground-state nonlattice potentials is

$$U_d^{(nl)} = U_3^{(nl)} - U_1^{(nl)} = \frac{|\alpha_f|}{16}(1 - \theta_n)(A_+^2 + A_-^2). \tag{12}$$

As we will see, the nonlattice potential leads to a dephasing of the signal.

The amplitudes $E_{\pm,0}$ can be related to the power $P_\pm$ in each of the beams via

$$E_{\pm,0} = \sqrt{\frac{16c\mu_0 P_\pm}{\pi w_{\pm,0}^2}}, \tag{13}$$

obtained by integrating the time-averaged Poynting vector in the $X = X_{\pm,0}$ planes. It is convenient to define

$$U_0 = \frac{1}{4}\alpha_g \frac{16c\mu_0 P}{\pi} \frac{1}{w_+(0)w_-(0)}, \tag{14}$$

where $X = 0$ denotes the position of the atomic cloud center, determined by the position of the magneto-optical trap, and

$$P = \sqrt{P_+ P_-}. \tag{15}$$

For matched ground-state and Rydberg lattice potentials, the ground- and Rydberg-state lattice potentials can be written in terms of U_0 as

$$U_g^{(l)}(\rho, X) \approx -U_0 \frac{w_+(0)w_-(0)}{w_+(X)w_-(X)}$$
$$\times e^{-\rho^2/w_+^2(X)} e^{-\rho^2/w_-^2(X)} \cos^2(k_L X) \tag{16}$$

and the differential shift resulting from the nonlattice potential as

$$U_d^{(nl)}(\rho, X) = \hbar\omega_d(\rho, X) = \frac{|\alpha_f|U_0}{2\alpha_g}(1 - \theta_n)\mathcal{I}(\rho, X), \tag{17}$$

where

$$\mathcal{I}(\rho, X) = \frac{w_+(0)w_-(0)}{2}$$
$$\times \left[\sqrt{\frac{1}{\xi}} \frac{e^{-2\rho^2/w_+^2(X)}}{w_+^2(X)} + \sqrt{\xi} \frac{e^{-2\rho^2/w_-^2(X)}}{w_-^2(X)}\right] \tag{18}$$

and $\xi = P_-/P_+$ is the ratio of reflected to incident power.

For different ground and Rydberg potentials, Eqs. (9) and (10) must be used for the lattice and nonlattice potentials, respectively. In our experiment, the atomic cloud is centered at $X = 0$ and

$$w_{+,0} = 33 \ \mu\text{m}, \quad w_{-,0} = 68 \ \mu\text{m},$$
$$X_{+,0} = 7.9 \ \text{mm}, \quad X_{-,0} = 23.9 \ \text{mm},$$
$$X_{+,r} = 3.35 \ \text{mm}, \quad X_{-,r} = 14.2 \ \text{mm},$$
$$\lambda_L \approx 1.02 \ \mu\text{m}, \quad \xi = 0.73. \tag{19}$$

B. Signal at the detector

The phase-matched signal recorded at a detector located at position $\mathbf{R}_d$ centered at a position along the positive X axis is proportional to a quantity S defined by

$$S = 2\epsilon_0 c R_d^2 \Omega_d \int dt \langle \mathbf{E}_-(\mathbf{R}_d) \cdot \mathbf{E}_+(\mathbf{R}_d)\rangle, \tag{20}$$

where Ω_d is the solid angle subtended by the detector and $\mathbf{E}_{\pm}(\mathbf{R}_d)$ are the positive and negative frequency components of the electric-field operator at the detector. The electric field arises from contributions from all the atoms.

To evaluate S, we must calculate the effects of the excitation field pulse, the retrieval (readout) field pulse, and the vacuum field on each atom and then sum the contribution from all atoms. A weak two-photon excitation pulse creates an atomic coherence for atom j characterized by a density matrix element $\rho_{31}^{(j)}$ at time $t = 0$. As a result of atomic motion and the nonlattice potential, this coherence undergoes dephasing. At time $t = T_s$, the retrieval pulse, taken as a square pulse that is in resonance with the 3-2 transition frequency, is applied to create the coherence $\rho_{21}^{(j)}$. The duration of the retrieval pulse is much longer than the lifetime $\tau_2 = 1/\gamma_2$ of level 2. The phase-matched signal emitted by the sample, which results from the interaction of the vacuum field with the atoms, is dependent on the value of $\rho_{21}^{(j)}$ created by the excitation and retrieval fields. If the Rabi frequency of the retrieval field is greater than γ_2, the signal is emitted in a time of order τ_2, which is assumed to be sufficiently short to neglect any dephasing while the signal is being emitted.

Using a calculation based on a source-field approach modified to allow for quantized motion of the atoms in the optical potentials, we find

$$S(T_s) = 2\epsilon_0 c \Omega_d \left(\frac{\omega_{21}^2 \mu_{21}}{4\pi\epsilon_0 c^2}\right)^2 \int_0^\infty d\tau$$
$$\times \left| \sum_j \sum_{q,q',q''}^{q_{max}} (A_{31}^{(j)}/2) \tilde{Q}^{(j)}(\tau) e^{-i\omega_d^{(j)} T_s} \rho_{1q'',1q'}(0) \right.$$
$$\left. \times M_{1q';3q}^{(j)}(-k\mathbf{u}_x) M_{3q;1q''}^{(j)}(k\mathbf{u}_x) e^{i(\omega_{q'}^{(j1)} - \omega_q^{(j3)})T_s} \right|^2, \quad (21)$$

where $k = (k_{E_1} - k_{E_2})$, μ_{21} is a dipole moment matrix element (it is assumed that the excitation and retrieval pulses are z polarized; the dipole moments that enter are also in the z direction), $A_{31}^{(j)} = \int_{-\infty}^{\infty} \Omega_{31}^{(j)}(t)dt$ is the pulse area of the excitation pulse whose two-photon Rabi frequency is defined by $\Omega_{31}^{(j)}(t) = \Omega_{E_1}^{(j)}(t)\Omega_{E_2}^{(j)}(t)/2\Delta_1$, $\rho_{qq'}(0)$ is an initial density matrix element for the motional lattice trap states, $\omega_d^{(j)}$ is given by

$$\omega_d^{(j)} = \left[U_3^{(nl)(j)} - U_1^{(nl)(j)}\right]/\hbar, \quad (22)$$

$$\tilde{Q}^{(j)}(\tau) = \frac{\Omega_{32}^{(j)}}{\sqrt{\Omega_{32}^{(j)2} - \gamma^2}} e^{-\gamma\tau/2} \sin\left[\frac{\sqrt{\Omega_{32}^{(j)2} - \gamma^2}}{2}\tau\right], \quad (23)$$

$$M_{3q;1q'}^{(j)}(\mathbf{k}) = \int dX_j [\psi_{3q}(X_j)]^* e^{i\mathbf{k}\cdot\mathbf{R}_j} \psi_{1q'}(X_j)$$
$$= [M_{1q';3q}(-\mathbf{k})]^*, \quad (24)$$

$\Omega_{32}^{(j)} = \Omega_R^{(j)}$ is the Rabi frequency of the retrieval pulse, $\psi_{\alpha q}(\mathbf{R}_j)$ is an eigenfunction and $\hbar\omega_q^{(j\alpha)}$ an eigenvalue for atom j moving in the potential $U_\alpha^{(j)}(X)$ ($\alpha = 1, 3$) given in Eqs. (9), $U_3^{(nl)(j)}$ ($\alpha = 1, 3$) are the nonlattice potentials

given in Eqs. (10), and all field strengths and frequencies now include the variation of field strength with location in the sample, indicated by the superscript (j). The sums over q, q', q'' are restricted to (quasibound) states; that is, q_{max} is the number of bound states in the potential.

C. Final expression for the signal

The numerical calculation of $S(T_s)$ is time consuming, since the sum over j in Eq. (21) must be carried out for each τ, the result squared, and then integrated over τ. To simplify matters, we assume that $\tilde{Q}^{(j)}(\tau)$ can be approximated as a function of τ times $\Omega_{32}^{(j)}$. We have verified that such an assumption leads to errors of at most 10% in the nonlattice potential contributions to $S(T_s)$ for times $T_s \lesssim 40$ μs. With this assumption, the signal at time T_s normalized to that at $T_s = 1$ μs can be written as

$$\eta(T_s) = G(T_s)/G(T_s = 1\,\mu\text{s}), \quad (25)$$

where

$$G(T_s) = \left| \int_{-\infty}^{\infty} dX \int_0^\infty \rho \, d\rho \, f(\rho, X) \mathcal{N}(\rho, X) C(\rho, X, T_s) \right|^2$$
$$\times e^{-T_s/\tau_{eff}}, \quad (26)$$

$$C(X, \rho, T_s) = \sum_{q,q',q''}^{q_{max}} e^{-i\omega_d(\rho,X)T_s} \rho_{1q'',1q'}(0) M_{1q';3q}[-k\mathbf{u}_x]$$
$$\times M_{3q;1q''}[k\mathbf{u}_x] e^{i(\omega_{q'}^{(1)} - \omega_q^{(3)})T_s}, \quad (27)$$

where $\mathcal{N}(\rho, X)$ and τ_{eff} are the atomic density distribution and the effective lifetime of the Rydberg level, respectively. The frequencies $\omega_{q'}^{(1)}$ and $\omega_q^{(3)}$ are implicit functions of ρ and X. The sum over j has been converted to a spatial integral over the sample.

The distribution $f(\rho, X)$ appearing in Eq. (26) is equal to the product of the spatially dependent envelopes of the excitation and retrieval electric-field amplitudes, namely,

$$f(\rho, X) = \left(\frac{w_{E_1,0}}{w_{E_1}(X)}\right) \exp\left[-\frac{\rho^2}{w_{E_1}^2(X)}\right]$$
$$\times \left\{\left(\frac{w_{E_2,0}}{w_{E_2}(X)}\right) \exp\left[-\frac{\rho^2}{w_{E_2}^2(X)}\right]\right\}^2, \quad (28)$$

where $w_{i,0}$ are the transverse waists of the beams at the foci, $w_i(X) = w_{i,0}\sqrt{1 + (\frac{X}{X_{ri}})^2}$, and X_{ri} is the Rayleigh length for beam i (we have taken equal Rayleigh lengths for fields E_2 and E_R). In our experiment,

$$w_{E_1,0} = 17\,\mu\text{m}, \quad w_{E_2,0} = 15\,\mu\text{m}. \quad (29)$$

It is assumed that the *transverse* motion is frozen on the time scale of the experiment. As a consequence, the atomic density is determined by the transverse Boltzmann distribution. The transverse trap potential is actually different for the ground and Rydberg levels. We will assume that the transverse density distribution is determined by the spatially averaged

[that is, with $\cos^2(k_L X) \to 1/2$] ground-state optical potential given in Eq. (4),

$$U_g(\rho, X) \approx -\frac{1}{16}\alpha_g[2A_+A_- + (A_+ - A_-)^2]$$

$$= -\frac{U_0\mathcal{I}(\rho, X)}{2}, \tag{30}$$

where $\mathcal{I}(\rho, X)$ is given in Eq. (18). Moreover, the $\theta \approx 5°$ angle between the excitation beams and the X axis results in an effective length L in the X direction of the atomic sample that we model using a Gaussian distribution. The transverse and longitudinal effects combine to produce an atomic density profile given by

$$\mathcal{N}(\rho, X) = \exp\left[\frac{U_0}{2k_BT}\mathcal{I}(\rho, X)\right]\exp\left[-\frac{X^2}{L^2}\right]. \tag{31}$$

The factor $C(X, \rho, T_s)$ in Eq. (27) is the product of a nonlattice contribution $e^{-i\omega_d(\rho,X)T_s}$ and a lattice contribution corresponding to motional dephasing. In principle, the motional dephasing term contains a ρ and X dependence owing to the spatial dependence of the frequencies $\omega_{q'}^{(1)}$ and $\omega_q^{(3)}$. However, for the Rayleigh lengths and waists of the trap fields used in our experiment, it is an excellent approximation to evaluate these frequencies at the center of the sample, $\rho = 0$ and $X = 0$. With this approximation the signal factors and can be written as

$$G(T_s) = G_{nl}(T_s)G_l(T_s)e^{-T_s/\tau_{\text{eff}}}, \tag{32}$$

where

$$G_{nl}(T_s) = \left|\int_{-\infty}^{\infty} dX \int_0^{\infty} \rho\, d\rho\, f(\rho, X)\mathcal{N}(\rho, X)e^{-i\omega_d(\rho,X)T_s}\right|^2, \tag{33}$$

$$G_l(T_s) = \left|\sum_{q,q',q''}^{q_{\max}} \rho_{1q'',1q'}(0)M_{1q';3q}(-k\mathbf{u}_x)\right.$$
$$\left.\times M_{3q;1q''}(k\mathbf{u}_x)e^{i(\omega_{q'}^{(1)}-\omega_q^{(3)})T_s}\right|^2, \tag{34}$$

and the frequencies $\omega_{q'}^{(1)}$ and $\omega_q^{(3)}$ are obtained as eigenvalues of the potentials

$$U_1^{(l)}(X) = -U_0\cos^2(k_LX), \tag{35a}$$

$$U_3^{(l)}(X) = -\frac{U_0}{\alpha_g}\cos^2(k_LX)\left[\frac{D_n^2}{6\hbar\Delta} - |\alpha_f|\theta_n\right], \tag{35b}$$

respectively.

The nonlattice contribution to the signal given in Eq. (33) is evaluated numerically. Owing to the fact that ω_d is a function of ρ and X, there is an inhomogeneous broadening in the sample that results in a decrease of $G_{nl}(T_s)$ with increasing T_s. To see the effect of the sample length on $G_{nl}(T_s)$, we plot in Fig. 2(a)

$$g_{nl}(T_s) = G_{nl}(T_s)/G_{nl}(0)$$

for $U_0/k_B = 32\,\mu$K ($U_0/h = 0.666$ MHz), $U_0/k_BT = 2.75$, $|\alpha_f|/\alpha_g = 0.628$, and $L = 1, 50, 100, 150$, and $500\,\mu$m. The integral over ρ leads to a decay of $g_{nl}(T_s)$, even for $L = 0$, owing to radial inhomogeneities in the nonlattice phase. With
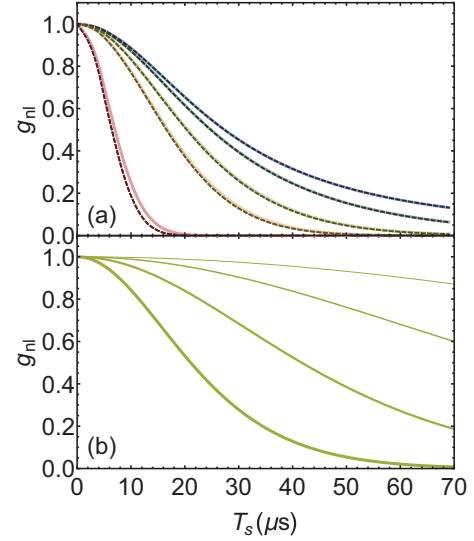

FIG. 2. (a) Graph of the analytic approximation and exact expressions of g_{nl} (dashed and solid curves, respectively) as a function of storage time T_s for $U_0/k_B = 40\,\mu$K and different sample lengths: blue, $L = 1\,\mu$m; dark green, $L = 50\,\mu$m; light green, $L = 100\,\mu$m; orange, $L = 150\,\mu$m; and red, $L = 500\,\mu$m. (b) Graph of g_{nl} for sample length $L = 100\,\mu$m and trap depths $U_0/k_B = 5, 10, 20$, and $40\,\mu$K, represented by increasing line thickness.

increasing L there is an additional contribution to the dephasing from the integral over X. It is evident from the figure that this contribution to the dephasing becomes important for $L \gtrsim 50\,\mu$m.

If the Rayleigh lengths for all the fields are much greater than L and if $w_\pm(0) \gg w_{E_{1,2},0}$, it is possible to get an analytic expression for $g_{nl}(T_s)$ that is in excellent agreement with the result obtained using numerical integration. To do so, we expand

$$\mathcal{I}(\rho, X) \approx \mathcal{I}(0, 0) + aX + b\rho^2, \tag{36}$$

where

$$a = \left.\frac{d\mathcal{I}(0, X)}{dX}\right|_{X=0}, \tag{37a}$$

$$b = \left.\frac{1}{2}\frac{d^2\mathcal{I}(\rho, 0)}{d\rho^2}\right|_{\rho=0}, \tag{37b}$$

and set $f(\rho, X) \approx f(\rho, 0)$. With these approximations the integrals in Eq. (33) can be calculated analytically. In this manner, we find

$$g_{nl}(T_s) \approx e^{-2T_s^2/\tau_X^2}\frac{1}{1 + \frac{T_s^2}{\tau_\rho^2}}, \tag{38}$$

where

$$\tau_X = \frac{2}{\frac{|\alpha_f|U_0}{2\alpha_g}(1 - \theta_n)aL}, \tag{39a}$$

$$\tau_\rho = \frac{1}{\frac{|\alpha_f|U_0}{2\alpha_g}(1 - \theta_n)b}\left(\frac{1}{w_{E_1,0}^2} + \frac{2}{w_{E_2,0}^2} - \frac{bU_0}{2k_BT}\right). \tag{39b}$$
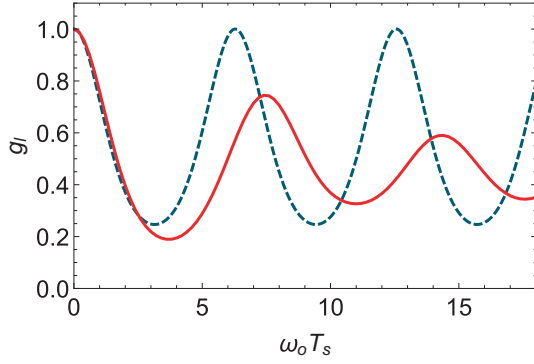
FIG. 3. Graph of $g_l(T_s)$ as a function of $\omega_0 T_s$: red solid curve, $\cos^2(k_L X)$ potential; black dashed curve, harmonic potential.

The Gaussian factor in Eq. (38) results from the longitudinal integration and the Lorentzian factor from the transverse integration. Equation (38) for $g_{nl}(T_s)$, plotted as the dashed curves in Fig. 2(a), is in very good agreement with the values of $g_{nl}(T_s)$ obtained from numerical integration of Eq. (33).

From Eqs. (39) it follows that the lifetimes decrease with increasing U_0. This feature is seen in Fig. 2(b), where $g_{nl}(T_s)$ is plotted for $L = 100\ \mu$m, $|\alpha_f|/\alpha_g = 0.628$, and $U_0/k_B = 5$, 10, 20, $40\ \mu$K, with the ratio $U_0/k_B T = 2.75$ kept fixed.

The motional dephasing contribution to the signal given in Eq. (34) is summed using a thermal ground-state distribution

$$\rho_{1q,1q'}(0) = \frac{\exp\left[-\frac{\hbar\omega_q^{(1)}}{k_B T}\right]\delta_{q,q'}}{\sum_{q=0}^{q_{\max}} \exp\left[-\frac{\hbar\omega_q^{(1)}}{k_B T}\right]}, \tag{40}$$

where $\delta_{q,q'}$ is a Kronecker delta. The $\omega_q^{(1)}$ are obtained by solving the appropriate Mathieu equation for the potentials given in Eqs. (35), limited to quasi-bound-state energies. The matrix elements needed in Eq. (34) have been calculated using the corresponding Mathieu wave functions. The values of θ_n used in fitting the data, calculated using a method to be described in the following section, are $\theta_n = 0.909$, 0.705, 0.334, 0.082, 0.059, -0.013, and -0.016 for $n = 30$, 40, 51, 59, 60, 65, and 70, respectively.

In Fig. 3 we plot

$$g_l(T_s) = G_l(T_s)/G_l(0) \tag{41}$$

as a function of $\omega_0 T_s$ for $U_0/k_B = 32\ \mu$K and $U_0/k_B T = 2.75$. The frequency ω_0 is defined by

$$U_0 = \frac{1}{2}\frac{M\omega_0^2}{k_L^2} \tag{42}$$

such that, for large ratios of $U_0/k_B T$ and small values of the trap Lamb-Dicke parameter $\eta_{LD} = k_L\sqrt{\hbar/2M\omega_0}$, the potentials should approximate those of an oscillator. Superimposed on the graph is a plot of $g_l(T_s)$ for oscillator potentials characterized by the same value of ω_0. It can be seen that the anharmonicity both damps the signal and reduces the fringe visibility that is obtained for harmonic potentials.

The expression for $G_l(T_s)$ can be cast in a suggestive form when the ground and Rydberg potentials are identical. In that limit, Eq. (27) reduces to

$$G_l(T_s) = |\langle e^{-ik\hat{X}(T_s)}e^{ik\hat{X}(0)}\rangle|^2, \tag{43}$$

where $\hat{X}(T_s)$ and $\hat{X}(0)$ are Heisenberg operators and the average is over the quantized motional states of an atom located at cloud center. We can take a classical limit of Eq. (43) by ignoring the commutator of $\hat{X}(T_s)$ and $\hat{X}(0)$ and replacing the operators by their classical counterparts $X(T_s)$ and $X(0)$ to arrive at

$$C_l \sim \langle e^{-ik[X(T_s)-X(0)]}\rangle, \tag{44}$$

where the average is now a classical average over the initial conditions. For our experimental parameters, the classical and quantum results do not differ by more than 10%.

We include three dissipative mechanisms that affect the ground-state–Rydberg coherence lifetime. The effective population decay lifetime is given by

$$\frac{1}{\tau_{\text{eff}}} = \frac{1}{\tau_{6p,n}} + \frac{1}{\tau_n^{(0)}} + \frac{1}{\tau_n^{(\text{bb})}}, \tag{45}$$

where $\tau_{6p,n}$, $\tau_n^{(0)}$, and $\tau_n^{(\text{bb})}$ are the contributions from the lattice-induced population decay of the $6p_{3/2}$ level, Rydberg level decay at zero temperature, and blackbody-induced transitions, respectively. Explicitly,

$$\tau_{6p,n} \approx \frac{\alpha_g}{U_0}\frac{24\hbar^2\Delta^2\tau_{6p,0}}{D_n^2(\xi^{-1/4}+\xi^{1/4})^2}$$

$$\tau_n^{(0)} = \tau^{(0)}(n^*)^{2.94},$$

$$\tau_n^{(\text{bb})} = \frac{3\hbar(n^*)^2}{4\alpha_{\text{FS}}^3 k_B T},$$

where $\tau_{6p,0} = 125$ ns, $\tau^{(0)} = 1.43$ ns, $T = 293$ K,

$$n^* = n - 3.13 \tag{46}$$

is the effective electronic quantum number, and α_{FS} is the fine-structure constant. At low n, the lifetime is limited mainly by spontaneous decay and blackbody transitions. With $n \gtrsim 40$, the dephasing produced by the nonlattice potential begins to reduce the lifetime, an effect that saturates for $n \gtrsim 60$. For still higher values of n, the lattice-induced population of the $6p_{3/2}$ begins to play an important role in limiting the coherence lifetime. The reason for this is that the magic detuning $\Delta_{m,n}$ decreases with increasing n.

The data have been fit using Eqs. (25), (32)–(34), (40), and (45) with $L = 100\ \mu$m. The potential depth is used as a free parameter to match the oscillation periods of the signals, while the temperature is chosen to match the fringe visibility.

D. Value of θ_n and reduced dipole moment matrix elements

1. Value of θ_n

The polarizability of the Rydberg level is affected by a breakdown of the electric dipole approximation due to the finite size of the Rydberg electron orbital. This landscape factor [31] is calculated by finding the expectation value of the periodic portion of the trap potential $\theta_n = \langle\cos(2k_L x)\rangle$, where k_L is the wave number of the lattice field and x

is the longitudinal position of the electron. To calculate θ_n we perform an expansion of $\cos(2k_L x)$ in spherical Bessel functions to obtain

$$\theta_n = (2l+1) \sum_{l'=\text{even}} (2l'^{l'/2-m_z}) \begin{pmatrix} l & l' & l \\ -m_z & 0 & m_z \end{pmatrix}$$

$$\times \begin{pmatrix} l & l' & l \\ 0 & 0 & 0 \end{pmatrix} \int_0^\infty dr_e P_{nl}^2(r_e) j_{l'}(2k_L r_e),$$

where the $j_{l'}(2k_L r_e)$ are spherical Bessel functions of the first kind and $P_{nl}(r_e)$ are the Rydberg radial wave functions calculated via Numerov integration of the Schrödinger equation using quantum-defect potentials. We only consider the $l=0$ term which simplifies the expression to

$$\theta_n = \int_0^\infty dr_e P_{n,0}^2(r_e) j_0(2kr_e).$$

2. Reduced dipole moment matrix elements

Using Eqs. (9)–(11), we can write the lattice potentials approximately as

$$U_1^{(l)}(X) = -U_0 \cos^2(k_L X), \tag{47a}$$

$$U_3^{(l)}(X) = -\frac{U_0}{\alpha_g} \cos^2(k_L X)$$

$$\times \left[(\alpha_g + |\alpha_f|\theta_n) \frac{\Delta_{m,n}}{\Delta} - |\alpha_f|\theta_n \right] \tag{47b}$$

and the nonlattice potential difference as

$$\hbar\omega_d(\rho, X) = \left[U_3^{(nl)} - U_1^{(nl)} \right] = \frac{|\alpha_f|U_0}{2\alpha_g}(1 - \theta_n)\mathcal{I}(\rho, X)$$

$$- \frac{U_0}{4} w_+(0)w_-(0)\left(1 + \frac{|\alpha_f|\theta_n}{\alpha_g}\right)\left(\frac{\Delta_{m,n}}{\Delta} - 1\right)$$

$$\times \left(\xi^{-1/4} \frac{1}{w_+(X)} e^{-\rho^2/w_+^2(X)} + \right.$$

$$\left. - \xi^{1/4} \frac{1}{w_-(X)} e^{-\rho^2/w_-^2(X)} \right)^2, \tag{48}$$

where $\Delta_{m,n}$ is the magic detuning for state ns. Owing to the anharmonicity of the potentials and the presence of a nonlattice potential, the local maxima of the signals do not necessarily occur exactly at $\Delta = \Delta_{m,n}$. To extract values for D_n, we find the value of $\Delta_{m,n}$ that gives the best fit to the experimental curves of signal strength versus Δ and then use

$$\frac{1}{6} \frac{D_n^2}{\hbar\Delta_{m,n}} = \alpha_g + |\alpha_f|\theta_n \tag{49}$$

to find D_n. The value of D_n is compared with the corresponding value calculated using wave functions obtained using the Alkali Rydberg Calculator (ARC) PYTHON package [32]. The ground-state polarizability was taken from Ref. [23].

III. EXPERIMENTAL RESULTS

The experimental geometry and measurement sequence are shown in Fig. 1(a). An optical lattice is formed by a
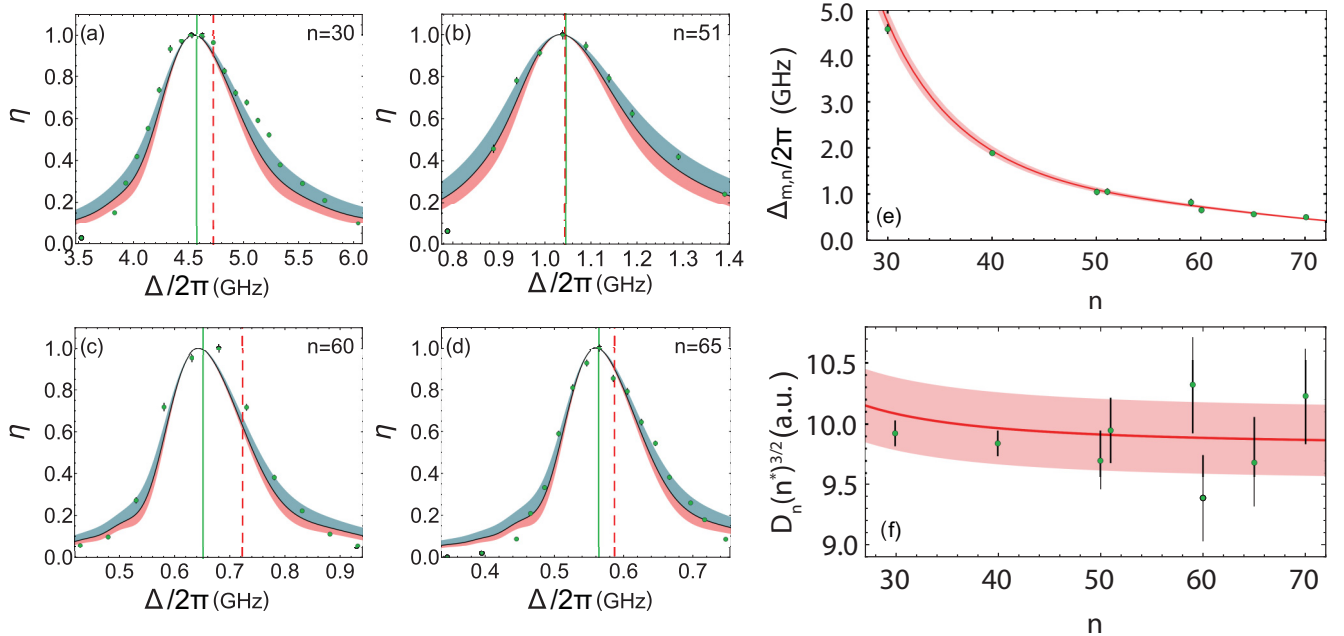

FIG. 4. (a)–(d) Normalized signal $\eta(T_s)$ at storage time T_s around the first revival (10–12 μs) as a function of lattice detuning Δ for principal quantum numbers 30, 51, 60, and 65. The solid curves, based on the model described in the text, are used to extract the values of $\Delta_{m,n}$. The dashed red and solid green vertical lines represent the theoretically expected and the extracted values of the magic detuning, respectively. Blue and red bands represent fits using temperatures 20% lower and higher than the best-fit value, respectively. (e) $\Delta_{m,n}$ as a function of the principal quantum number n, with the solid curve based on our theoretical model. (f) Extracted values of the scaled reduced matrix elements as a function of n.

y-polarized, retroreflected laser field propagating along the x axis having power $P_+ \approx 0.8$ W. The trap field is generated by a titanium-sapphire laser tunable in the (850–1050)-nm range, frequency locked to an optical cavity. The laser wavelength is measured with a wave meter calibrated to 10-MHz accuracy using a diode laser locked to the Rb 780-nm line. The trap field is detuned from $\omega_{ns,6p_{3/2}}$ by Δ.

Atoms are loaded into the lattice using a magneto-optical trap. The maximum depth of the optical dipole potential at the atoms is $U_0/k_B \approx 40$ μK, with the corresponding axial and radial oscillation frequencies $\{v_\rho, v_X\} \approx \{0.3, 80\}$ kHz. The resulting cloud, which has temperature of $T \approx 10$ μK, consists of $\sim 10^5$ ^{87}Rb atoms having radial and axial waists of $\sigma_\rho \approx 50$ μm and $\sigma_X \approx 0.2$ mm, respectively. The atoms are optically pumped to the $|5S_{1/2}, F = 2, m_F = 0\rangle$ state in a magnetic bias field $B_0 = 0.5$ mT.

Two nearly counterpropagating z-polarized fields E_1 and E_2 excite a spin wave between the $|5s_{1/2}, F = 2\rangle$ and $|ns_{1/2}\rangle$ levels. The fields imprint a spatial phase coherence between the ground and Rydberg states varying as proportional to $e^{i(\vec{k}_1+\vec{k}_2)\cdot\vec{R}}$, where $\vec{k}_1$ and $\vec{k}_2$ are the wave vectors for the fields

E_1 and E_2, respectively. The field E_1 has a wavelength of 420 nm, while the field E_2, produced by a laser diode, is tunable in the (1012–1026)-nm wavelength range to excite Rydberg states with principal quantum numbers $n \geqslant 30$. The field E_2 is detuned from $\omega_{ns,6p_{3/2}}$ by $\Delta_1/2\pi \approx 12$ MHz. The E_1 and E_2 fields are focused onto the atoms with beam waists $w_{E_1,0} \approx 17$ μm and $w_{E_2,0} \approx 15$ μm and Rabi frequencies $\Omega_{E_1}/2\pi \simeq 0.2$ MHz and $\Omega_{E_2}/2\pi \simeq 5$ MHz, respectively. The spin wave is stored for a period T_s varied between 1 and 70 μs. At time T_s the atoms are resonantly driven on the $|ns_{1/2}\rangle \leftrightarrow |6p_{3/2}\rangle$ transition by a (z-polarized) retrieval field E_R of Rabi frequency $\Omega_R \approx \Omega_{E_2}$, creating an array of atomic dipoles which give rise to a phase-matched emission from the sample. The emitted light is collected into a single-mode optical fiber coupled to a single-photon detector. To avoid damaging the detectors by the E_1 field, a gating acousto-optical modulator is used. The photon transmission and detection efficiency η_{td} is given by $\eta_{td} = \eta_c\eta_o\eta_f\eta_d = 0.13$, where $\eta_c = 0.89$, $\eta_o = 0.39$, $\eta_f = 0.66$, and $\eta_d = 0.55$ are the vacuum cell transmission efficiency, optics transmission efficiency (including the gating acousto-optic modulator), fiber coupling efficiency, and single-photon detection efficiency, respectively. The arrival times of detected photons are recorded and the number of detected photons per excitation and retrieval cycle is used as our signal.
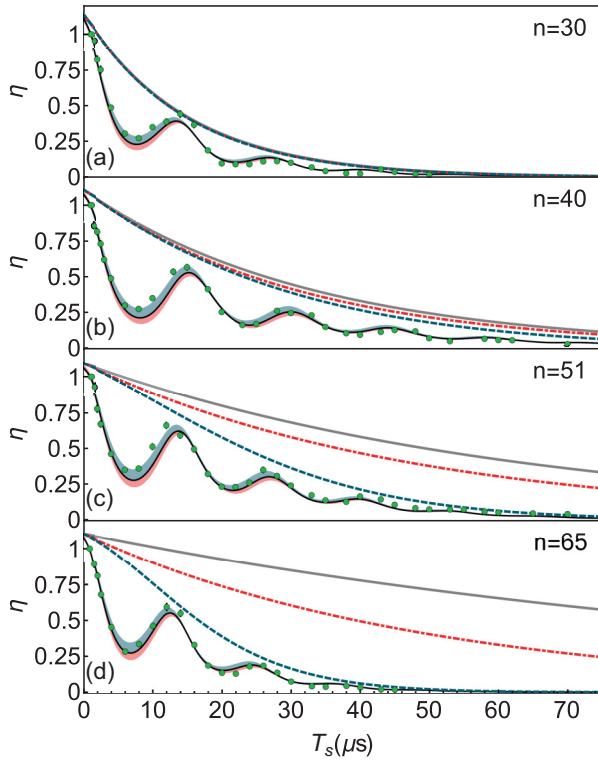
A. Magic wavelengths for the 5s-ns transition

The normalized retrieval signal $\eta(T_s)$, given by Eq. (25), is plotted in Figs. 4(a)–4(d) as a function of Δ, along with the experimental data points. The solid green vertical lines represent the values of the magic detunings $\Delta_{m,n}$ extracted from the fit of the theoretical curves to the data, while the dashed red vertical lines represent the values of $\Delta_{m,n}$ obtained using Eq. (49) and the ARC values of the dipole matrix elements. The extracted values of $\Delta_{m,n}$ are plotted in Fig. 4(e). Consistent with the scaling of dipole matrix elements, $\Delta_{m,n}$ varies approximately as $(n^*)^{-3}$. The values of $D_n(n^*)^{3/2}$ obtained from Eq. (49) using the extracted values of $\Delta_{m,n}$ are shown in Fig. 4(f), superimposed on the expected values of the matrix elements computed using the ARC values [32]. The 3% standard deviation band is based on comparing our computed values of $|\langle 15s_{1/2}||\hat{d}||np\rangle|$ reduced matrix elements with the values for these matrix elements given in Ref. [23].

B. Dynamics of the ground-state–Rydberg coherence

The signal as a function of T_s serves as a measure of the dynamics of the stored spin wave. With $\Delta = \Delta_{m,n}$, the signal as a function of storage time T_s, normalized to its value at $T_s = 1$ μs, is plotted in Fig. 5, along with the theoretical curves. The oscillations result from the nearly periodic motion of the atoms along the optical lattice. The oscillation visibility decreases with time owing to the anharmonic nature of the potential. Moreover, the anharmonicity adds a small damping component to the signal and its contribution becoming more pronounced with increasing temperature.

In Fig. 6 we compare the $n = 40$ signal with its counterpart obtained by exciting the atoms with 795- and 475-nm fields via the $|5p_{1/2}, F = 1\rangle$ intermediate level. The effective

FIG. 5. Normalized signal η as a function of storage time for several principal quantum numbers: (a) $n = 30$, (b) $n = 40$, (c) $n = 51$, and (d) $n = 65$. The solid black curve is based on our theoretical model. Blue and red bands represent temperatures 20% lower and higher than the best-fit value, respectively. The gray curve shows loss attributable to blackbody and spontaneous decay from the Rydberg state. The dashed red curve adds in the contribution of spontaneous decay from the $6P$ level. The dashed blue curve additionally includes the dephasing attributable to the nonlattice potential. Most experimental error bars are smaller than the shown markers.
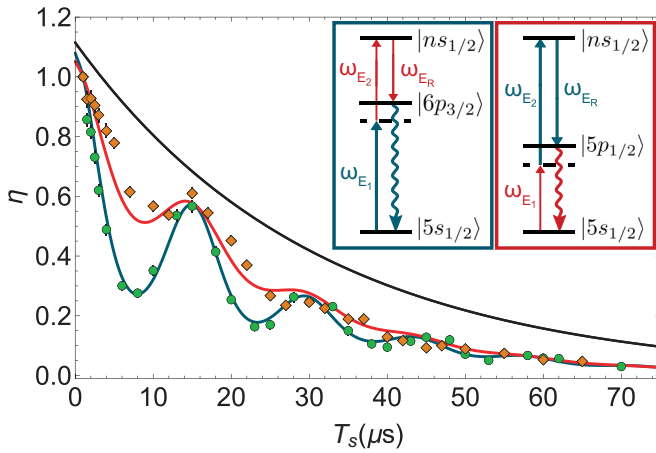
FIG. 6. Normalized signal η as a function of storage time for $n = 40$ for (420–1018)-nm (green circles) and (795–475)-nm (orange diamonds) excitation, with the corresponding atomic transitions shown in the inset. The solid curves are the result of a numerical simulation of atomic motion using the model described in the text. The black curve is the same as in Fig. 5. Most experimental error bars are smaller than the shown markers.

two-photon excitation wavelength for the latter $\lambda_{2ph} = 1.2$ μm, longer than the $\lambda_{2ph} = 0.72$ μm for the (420–1018)-

nm excitation. As one would expect, the (795–475)-nm excitation exhibits lower visibility of oscillations as a result of decreased motional dephasing for the longer-wavelength spin wave. The role of trap anharmonicity also decreases with longer spin-wave period, whereas the nonlattice contribution to the dephasing contribution is unaffected by it.

IV. CONCLUSION

We have demonstrated ground-state–Rydberg atomic coherence lifetimes in excess of 20 μs using a state insensitive optical lattice. A theory has been developed to account for the quantized motion of atoms in the trap potentials. The theoretical line shapes that are derived are in good agreement with the experimental results and can be used to extract values for the ns-$6p_{3/2}$ reduced electric dipole matrix elements. Our approach should be of use for precision measurements and quantum information studies involving atomic Rydberg states.

ACKNOWLEDGMENTS

[1] T. F. Gallagher, *Rydberg Atoms* (Cambridge University Press, Cambridge, 1994).

[2] M. Saffman, T. G. Walker, and K. Mølmer, Rev. Mod. Phys. **82**, 2313 (2010).

[3] M. D. Lukin, M. Fleischhauer, R. Cote, L. M. Duan, D. Jaksch, J. I. Cirac, and P. Zoller, Phys. Rev. Lett. **87**, 037901 (2001).

[4] M. Saffman and T. G. Walker, Phys. Rev. A **66**, 065403 (2002).

[5] P. Kómór, T. Topcu, E. M. Kessler, A. Derevianko, V. Vuletić, J. Ye, and M. D. Lukin, Phys. Rev. Lett. **117**, 060506 (2016).

[6] B. Zhao, M. Müller, K. Hammerer, and P. Zoller, Phys. Rev. A **81**, 052329 (2010).

[7] E. Brion, F. Carlier, V. M. Akulin, and K. Mølmer, Phys. Rev. A **85**, 042324 (2012).

[8] Y. Han, B. He, K. Heshami, C.-Z. Li, and C. Simon, Phys. Rev. A **81**, 052311 (2010).

[9] Y. O. Dudin and A. Kuzmich, Science **336**, 887 (2012).

[10] Y. O. Dudin, L. Li, F. Bariani, and A. Kuzmich, Nat. Phys. **8**, 790 (2012).

[11] D. Maxwell, D. J. Szwer, D. Paredes-Barato, H. Busche, J. D. Pritchard, A. Gauguet, K. J. Weatherill, M. P. A. Jones, and C. S. Adams, Phys. Rev. Lett. **110**, 103001 (2013).

[12] L. Li, Y. O. Dudin, and A. Kuzmich, Nature (London) **498**, 466 (2013).

[13] T. Peyronel, O. Firstenberg, Q.-Y. Liang, S. Hofferberth, A. V. Gorshkov, T. Pohl, M. D. Lukin, and V. Vuletić, Nature (London) **488**, 57 (2012).

[14] O. Firstenberg, T. Peyronel, Q.-Y. Liang, A. V. Gorshkov, M. D. Lukin, and V. Vuletić, Nature (London) **502**, 71 (2013).

[15] S. Baur, D. Tiarks, G. Rempe, and S. Dürr, Phys. Rev. Lett. **112**, 073901 (2014).

[16] D. Tiarks, S. Baur, K. Schneider, S. Dürr, and G. Rempe, Phys. Rev. Lett. **113**, 053602 (2014).

[17] H. Gorniaczyk, C. Tresp, J. Schmidt, H. Fedder, and S. Hofferberth, Phys. Rev. Lett. **113**, 053601 (2014).

[18] M. Ebert, A. Gill, M. Gibbons, X. Zhang, M. Saffman, and T. G. Walker, Phys. Rev. Lett. **112**, 043602 (2014).

[19] D. Barredo, S. Ravets, H. Labuhn, L. Béguin, A. Vernier, F. Nogrette, T. Lahaye, and A. Browaeys, Phys. Rev. Lett. **112**, 183002 (2014).

[20] Y.-Y. Jau, A. M. Hankin, T. Keating, I. H. Deutsch, and G. W Biedermann, Nat. Phys. **12**, 71 (2016).

[21] J. Zeiher, R. van Bijnen, P. Schauß, S. Hild, J.-y. Choi, T. Pohl, I. Bloch, and C. Gross, Nat. Phys. **12**, 1095 (2016).

[22] H. Bernien *et al.*, Nature (London) **551**, 579 (2017).

[23] M. S. Safronova, C. J. Williams, and C. W. Clark, Phys. Rev. A **67**, 040303 (2003).

[24] M. Saffman and T. G. Walker, Phys. Rev. A **72**, 022347 (2005).

[25] E. A. Goldschmidt, D. G. Norris, S. B. Koller, R. Wyllie, R. C. Brown, J. V. Porto, U. I. Safronova, and M. S. Safronova, Phys. Rev. A **91**, 032518 (2015).

[26] P. R. Berman and V. S. Malinovsky, *Principles of Laser Spectroscopy and Quantum Optics* (Princeton University Press, Princeton, 2011), Chaps. 10 and 19.

[27] See, for example, S. Wu, P. S. Striehl, and M. G. Prentiss, arXiv:0710.5479; R. H. Leonard and C. A. Sackett, Phys. Rev. A **86**, 043613 (2012).

[28] R. Zhao, Y. O. Dudin, S. D. Jenkins, C. J. Campbell, D. N Matsukevich, T. A. B. Kennedy, and A. Kuzmich, Nat. Phys. **5**, 100 (2009).

[29] S. D. Jenkins, T. Zhang, and T. A. B. Kennedy, J. Phys. B **45**, 124005 (2012)

[30] T. Topcu and A. Derevianko, Phys. Rev. A **88**, 042510 (2013).

[31] T. Topcu and A. Derevianko, Phys. Rev. A **88**, 043407 (2013).

[32] N. Šibalić, J. D. Pritchard, C. S. Adams, and K. J. Weatherill, Comput. Phys. Commun. **220**, 319 (2017).